Hydrodynamics of viscous inhalant flows

Aaron C. True* and John P. Crimaldi†

Department of Civil, Environmental and Architectural Engineering, University of Colorado Boulder, Boulder, Colorado 80309-0428, USA

(Received 1 February 2017; published 17 May 2017)

Inhalant flows draw fluid into an orifice from a reservoir and are ubiquitous in engineering and biology. Surprisingly, there is a lack of quantitative information on viscous inhalant flows. We consider here laminar flows (Reynolds number Re $\leqslant$ 100) developing after impulsive inhalation begins. We implement finite element simulations of flows with varying Re and extraction height h (orifice height above a bottom bed). Numerical results are experimentally validated using particle image velocimetry measurements in a physical model for a representative flow case in the middle of the Re-h parameter space. We use two metrics to characterize the flow in space and time: regions of influence (ROIs), which describe the spatial extent of the flow field, and inhalation volumes, which describe the initial distribution of inhaled fluid. The transient response for all Re features an inviscid sinklike component at early times followed by a viscous diffusive component. At lower Re, diffusion entrains an increasing volume of fluid over time, enlarging the ROI indefinitely. In some geometries, these flows spatially bifurcate, with some fluid being inhaled through the orifice and some bypassing into recirculation. At higher Re, inward advection dominates outward viscous diffusion and the flow remains trapped in a sinklike state. Both ROIs and inhalation volumes are strongly dependent on Re and extraction height, suggesting that organisms or engineers could tune these parameters to achieve specific inhalation criteria.

DOI: 10.1103/PhysRevE.95.053107

I. INTRODUCTION

In this study we investigate the hydrodynamics of a class of flows that we refer to as inhalant flows. In the most general sense, inhalant flows feature fluid drawn from an effectively infinite reservoir through an inlet orifice and into an inhalant tube (Fig. 1). These flows are ubiquitous in engineered and biological systems and yet while constituent aspects of this flow have been studied extensively in the literature in a variety of disparate contexts, there remains a surprising lack of quantitative information about the fundamental hydrodynamics, particularly for viscous flow approaching the inlet orifice. Here we consider laminar inhalant flows that develop following the impulsive start of constant volumetric inhalation.

Inhalant flows are common to many fields and they are referred to and intuitively understood through discipline-specific lenses. Engineers think of siphons as a means of conveying liquids into tubes and siphons are prototypical flows in the study of engineering hydraulics [1]. Biological oceanographers think of siphon and suction flows in the context of organismal feeding, predation, and respiration [2–4]. In the biomedical world, researchers refer to inspiratory flows in the context of respiration [5,6]. Scientists across disciplines use the term pipette [7] in reference to drawing a sample volume of fluid into a tube from a larger reservoir [8,9].

Conceptually, inhalant flows can be divided into three regions: the exterior flow upstream of the inlet orifice, the developing entrance flow just downstream of the inlet orifice, and the fully developed flow that follows. We refer to the latter two regions collectively as interior flow. The coupled interior and exterior flows upstream and downstream of the inlet orifice affect and inform the hydrodynamics of the holistic system. For example, terrestrial vertebrate respiration features inhalation of air through an inlet orifice (e.g., a nostril). Although some researchers have focused on the interior flow in the internal airways [5] and others have focused on aspects of the exterior flow [10], fundamental hydrodynamics of the coupled inhalant flow system have not been characterized, though they are certainly acknowledged [11]. While both interior flow regions have been investigated extensively in the literature, viscous exterior flow approaching an inlet orifice is relatively unstudied.

Exterior flows approaching an inlet orifice have been investigated in a variety of contexts; however, most studies feature simplifications and/or complexities that render a mechanistic understanding of viscous inhalant flow hydrodynamics impossible. For example, aerosol and water samplers both feature fluid drawn from an effectively infinite reservoir and considerable effort has gone into understanding optimal sampling procedures to eliminate biases associated with various inhalation regimes. These studies are predominantly conducted in the context of sampling particle-laden flows [12,13], however, and have not characterized the fundamental hydrodynamics, particularly for viscous flows in the exterior. Synthetic jets (net-zero mass flux) that produce periodic suction (inhalation) and ejection (exhalation) of fluid through an orifice are used in a variety of applications, including aerodynamic flow control [14] and turbulence generation [15], in which the interior flow is of little consequence. Biologically, various aspects of the exterior flow have been investigated in the context of organismal predation, feeding, and respiration [4]. Ambush-feeding fishes use impulsive suction to capture prey in a hydrodynamically inconspicuous manner [16,17]; while these studies do provide insight into some aspects of the exterior flow, they are often highly inertial and feature additional complexities such as dynamic inlet orifice geometries (mouth gape). Other aquatic organisms such as benthic bivalves (clams and oysters) draw prey- and oxygen-rich water through an inhalant siphon and expel the filtrate as an excurrent jet [3,18,19]; although these phenomena

*aaron.true@colorado.edu
†john.crimaldi@colorado.edu

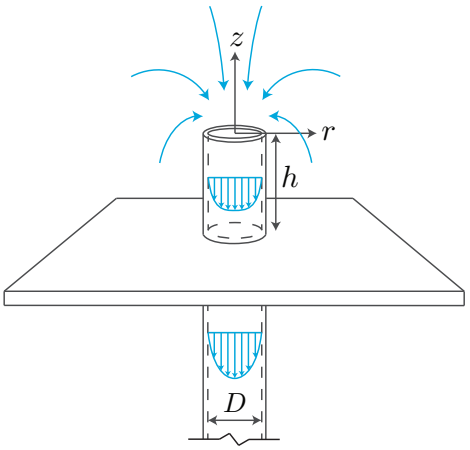

FIG. 1. Conceptual model of a generic inhalant flow. An inhalant tube of diameter D protrudes a distance h (the extraction height) above a flat plate into an infinite reservoir. Viscous fluid is drawn from the reservoir into the inhalant tube under the action of suction. A laminar velocity profile develops downstream of the inlet orifice.

are well documented morphologically and physiologically, characteristics of exterior flows generated by inhalant siphons are not well known.

Analytical treatment of exterior flow almost universally utilizes potential flow theory to produce an inviscid sink flow approximation, regardless of Reynolds number. For an inviscid point sink of strength $Q[L^3/T]$, the corresponding radial flow field $u_r(a)$ at radial distance a (spherical polar coordinate system) from the sink is

$$u_r(a) = -\frac{Q}{\alpha\pi a^2}, \tag{1}$$

where $\alpha = \text{const}$. For the limiting case of large extraction height ($h/D \gg 1$), the influence of the bottom bed is negligible and the exterior flow is typically approximated as a sink flow in an infinite domain with $\alpha = 4$. For the other limiting case when the inlet orifice is flush with the bottom bed ($h/D = 0$), the exterior flow approximation is a sink flow in a semi-infinite domain with $\alpha = 2$. These potential flow characterizations are inviscid and steady, lacking dependence on viscosity or time, and thus they are inherently incapable of describing time-evolving, viscous, inhalant flows [4]; these flows are fundamentally diffusive in nature, featuring fluid momentum diffusing radially outward from the inlet orifice. Although potential flows can satisfy impermeability boundary conditions, they are incapable of satisfying the viscous no-slip condition and therefore cannot resolve realistic boundary conditions.

Analytical solutions do exist for the idealized problem of axisymmetric flow generated by a point sink in the center of an infinite plate [20,21], or more generally at the vertex of a cone [22]. These solutions are of the matching type, however, featuring an inner laminar boundary layer flow matched to a potential outer flow; they are only valid in close proximity to the solid surface in the high-Re limit. As in all sink flows, these solutions are singular at the origin and break down in the neighborhood of the inlet orifice. They are ultimately incapable of describing inhalant flow hydrodynamics that feature viscous fluid flow in an effectively infinite domain forced by a directional and spatially distributed flow boundary condition at the inlet orifice.

Downstream of the inlet orifice, many facets of the problem of laminar interior flow have been extensively studied numerically, experimentally, and analytically. In the hydrodynamic entrance-length problem [23], the entrance (or development) length for inhalant flows is defined as the region of the interior flow over which the boundary layer grows from zero thickness at the inlet orifice to a thickness equal to the internal radius of the inhalant tube. In this region, flow develops from an initial velocity profile prescribed as a boundary condition at the inlet orifice to a fully developed profile invariant in the streamwise direction [24,25]. Typically the boundary condition prescribed at the inlet orifice is a uniform profile across the inlet, although some investigators have prescribed various other profiles (e.g., parabolic); the choice of boundary condition at the inlet determines the subsequent entrance length and associated pressure drop [26]. Even though the entrance-length problem has been extensively studied, there remains notable discrepancies between theory and experiment (reviewed by Durst *et al.* [23]).

Downstream of the developing flow in the entrance region, the Hagen-Poiseuille law governing steady laminar flow in an axisymmetric tube has been well known for close to 175 yr (see the history of Poiseuille's law by Sutera and Skalak [27]). Flow is driven through an axisymmetric tube of constant cross section under the influence of an axial pressure gradient ΔP. The velocity profile $w(r)$ in a tube of inner radius R is parabolic in the radial (r) direction and invariant in the axial (z or streamwise) direction (cylindrical polar coordinate system) as

$$w(r) = -\frac{\Delta P}{4\mu}(R^2 - r^2), \tag{2}$$

where μ is the fluid dynamic viscosity. The volumetric flow rate Q is

$$Q = -\frac{\Delta P \pi r^4}{8\mu}, \tag{3}$$

with the average cross-sectional velocity $w_o = Q/A$ over the cross-sectional tube area $A = \pi R^2$. Finally, the flow Reynolds number Re based on the inhalant tube inner diameter D for a fluid with kinematic viscosity ν is

$$\text{Re} = \frac{w_o D}{\nu}. \tag{4}$$

As detailed above, while various aspects of the exterior and interior flows have been investigated separately in a variety of contexts, the detailed hydrodynamics of the holistic problem, particularly for time-developing viscous flow approaching the inlet orifice, are not well known.

Historical treatment of the exterior inhalant flow as an inviscid sink flow, regardless of Re, is not unreasonable considering that analytical solutions to the Navier-Stokes equations are generally possible only in two limiting cases: in the low-Re ($\ll 1$) limit where the nonlinear advective terms vanish and in the high-Re limit ($\gg 1$) where viscous effects are negligible everywhere except in thin layers near solid surfaces (the viscous boundary layer). For intermediate Re where both viscosity and inertia are dynamically important throughout the

domain as in the present study, finding analytical solutions is impractical and we are forced to rely on experimental observation or numerical solutions applicable to specific geometries [21,28].

In this study we characterize the hydrodynamics of time-evolving viscous inhalant flows approaching an inlet orifice from an effectively infinite reservoir. We use numerical simulations to solve the viscous Navier-Stokes equations with realistic boundary conditions. We use the impulsive application of a constant volumetric inhalation rate Q to drive the time-evolving interior and exterior flows. We explore effects of Reynolds number and extraction height on the development of the exterior flow field and the spatial extent of fluid inhalation volumes.

II. METHODOLOGY

A. Flow description

We model laminar inhalant flows with fluid of density ρ and kinematic viscosity ν being drawn from an infinite reservoir into a round inhalant tube with inner diameter D and an inlet orifice at extraction height h above a solid bottom bed (Fig. 1). The flow develops in time and space following an impulsive start of constant volumetric flow rate Q within the inhalant tube. Viscous fluid is drawn from the reservoir into the inhalant tube under the action of suction and a laminar velocity profile develops downstream of the inlet orifice. We consider three Reynolds numbers (Re = 1, 10, and 100) and three extraction heights ($h = 0$, $2D$, and $40D$). The inhalant tube wall thickness is $0.1D$. The model is axisymmetric in a cylindrical polar coordinate system with origin at the center of the inlet orifice; z is axial distance from the inlet orifice and r is radial distance from the inhalant tube axis. The parameter space was chosen to investigate effects of viscosity and solid-bed interactions on the flow. The Re values range from a more viscous case (Re = 1) to one that approaches the inviscid limit while remaining well within the laminar regime (Re = 100). The extraction heights range from the limiting case of a bed-flush inlet orifice ($h = 0$) to the large-height limiting case ($h = 40D$) beyond which the effect of the solid bottom bed vanishes. Model results were insensitive to h for $h \geqslant 40D$.

B. Governing equations and scaling

The nondimensional flow field $\boldsymbol{u}^* = [u^*, w^*]$ with radial (r^*) and axial (z^*) velocity components u^* and w^* is governed by the nondimensional, incompressible, Navier-Stokes, and continuity equations

$$\frac{\partial \boldsymbol{u}^*}{\partial t^*} + \boldsymbol{u}^* \cdot \nabla^* \boldsymbol{u}^* = -\nabla^* p^* + \mathrm{Re}^{-1} \nabla^{*2} \boldsymbol{u}^* + \mathbf{g}^* \qquad (5)$$

and

$$\nabla^* \cdot \boldsymbol{u}^* = 0, \qquad (6)$$

where length, time, velocity, and pressure have been nondimensionalized by D, D/w_o, w_o, and ρw_o^2, respectively, and where $\mathbf{g}^* = D\mathbf{g}/w_o^2$. Note that the flow field governed by Eqs. (5) and (6) is controlled by the single nondimensional parameter Re [Eq. (4)]. Here and elsewhere we denote vector quantities in boldface, scalar quantities in lightface, and nondimensional quantities with an asterisk.

The initial conditions were zero velocity and pressure everywhere. The flow was started impulsively by a boundary condition of laminar outflow from the downstream end of the inhalant tube with constant volumetric flow rate $Q = w_o A$ at time $t^* \geqslant 0$. The inhalant tube walls and the bottom bed were impermeable no-slip boundaries. The top and lateral boundary conditions were open boundaries through which fluid could enter and leave the domain without normal stress. The implementation of the equations governing the initial and boundary conditions are described in detail in Sec. II C.

When nondimensionalizing the Navier-Stokes equations, the time scale for unsteadiness is $T = D/w_o$. This time scale has several useful context-specific interpretations. For example, rewriting the time scale as $T = D/w_o = (D^2/\nu)/\mathrm{Re}$ (where D^2/ν is the diffusive time scale) demonstrates that the transient time scale decreases with increasing Re. Alternatively, the time scale can be algebraically manipulated as $T = D/w_o = \pi D^3/4Q$, indicating that it is also the time required to pump a characteristic volume $(\pi/4)D^3$ (a cylinder with length and diameter D) through the inhalant tube at volumetric flow rate Q.

C. Numerical methods

Numerical simulations were performed via finite element discretization of the Navier-Stokes and continuity equations [Eqs. (5) and (6)]. Because the flow is driven entirely by a boundary condition of constant volumetric flow rate at the tube outlet, gravity plays no dynamical role and acts only to superimpose a hydrostatic pressure gradient. For this reason, we do not include gravity in the the finite element model formulation. The COMSOL MULTIPHYSICS package was used to generate the mesh and to solve the system of equations resulting from the weak (integral) form discretization of the governing equations. The mesh contained triangular and quadrilateral elements with local refinement around solid surfaces (inhalant tube walls and impermeable bottom bed). A mesh refinement study was performed to test for solution convergence throughout the domain. We iterated to finer meshes (increasing model degrees of freedom) until the total relative error estimate summed over all elements and degrees of freedom was of order 1×10^{-11} and there was no discernible change in the solution with further grid refinement. The final mesh implemented had typical maximum and minimum element sizes (spatial resolution) of approximately $0.075D$ and $0.01D$, respectively. In addition to the mesh refinement study, we also validated the model experimentally as discussed in detail below.

Lagrangian (polynomial) shape functions (basis functions) were implemented for weak form discretization of the fluid velocity (second-order) and pressure (first-order) fields; the second-order velocity shape functions are appropriate for the low flow velocities in the exterior laminar flow approaching the inlet orifice [29]. The order of the numerical integration scheme was matched to the order of the element

(shape function) for each dependent variable. The time discretization scheme was an implicit backward differentiation formula method with maximum second-order schemes, balancing numerical stability and damping tendencies for our gradually varying flows with smooth gradients. Backward differentiation formula methods use variable-order, variable-step-size backward differentiation and are known for their stability [30,31]. Time stepping was thus adaptive and the variable step size taken by the solver was informed by a prescribed absolute tolerance for the nonlinear solver and an implicit formulation of the mesh Courant-Friedrichs-Lewy number. The nonlinear systems of equations were solved using the direct PARDISO solver [32,33], a solver optimized for parallelized solution of sparse systems of equations.

Initial conditions were zero velocity and pressure everywhere, $\boldsymbol{u}^* = 0$ and $p^* = 0$. The inhalant tube walls and the bottom bed were impermeable no-slip conditions $\boldsymbol{u}^* = 0$. Flow was initiated by a boundary condition of constant volumetric flow rate Q from the downstream outlet of the inhalant tube for time $t^* \geqslant 0$. This was enforced by prescribing an outlet boundary condition of laminar outflow perpendicular to the flat boundary of the tube cross section with average outlet velocity $w_o = Q/A$. Laminar outflow is then prescribed via a coupled ordinary differential equation that computes p^*_{exit} such that the desired outlet velocity is achieved under laminar flow conditions: $L_{\text{exit}}\nabla_t^* \cdot \{-p^*\mathbf{I} + \mu[\nabla_t^*\boldsymbol{u}^* + (\nabla_t^*\boldsymbol{u}^*)^T]\} = -p^*_{\text{exit}}\mathbf{n}$, where $\mathbf{I}$ is the identity matrix, ∇_t^* is the tangential gradient, and $\mathbf{n}$ is the unit vector normal to the outlet boundary. This laminar outflow boundary condition is effectively a normal stress condition, together with a no tangential stress condition, a typical formulation for an outlet boundary condition [34]. The downstream outlet of the inhalant tube is located a distance L_{exit} downstream of the inlet orifice. To eliminate influence of outlet boundary conditions on exterior and interior flows of interest, L_{exit} is set as 10 times the empirical estimate of the low-Re, laminar, entry-flow development length [23].

In order to obtain a numerically well-posed problem and avoid convergence problems when specifying the desired velocity condition at the outlet, the inlet boundary conditions (top and lateral boundaries) were prescribed as pressure conditions [34]. Thus, the top and lateral domain boundaries were open boundaries through which fluid could enter and leave the domain without normal stress, prescribed as $\{-p^*\mathbf{I} + \mu[\nabla^*\boldsymbol{u}^* + (\nabla^*\boldsymbol{u}^*)^T]\}\mathbf{n} = 0$. Specifying zero normal force enforces that the pressure is balanced by the viscous shear force on the inlet boundaries, which is true when the normal gradient of the normal velocity at the boundary is small.

Fluid inhalation volumes were computed numerically by seeding passive particles across the inlet orifice and advecting them backward in time (improved Euler method) within flow fields solved for previously via numerical simulations of the Navier-Stokes equations. Refinement studies on spatial and temporal resolution of velocity data used to compute inhalant volumes ensured convergence. The shape and total volume of fluid captured are functions of the start time and inhalation period. Inhalation volumes were computed with a start time $t^* = 100$, well beyond the time scale of rapid transient development ($t^* = 1$), and proceeded for a total inhalation period of $\Delta t^* = 100$.

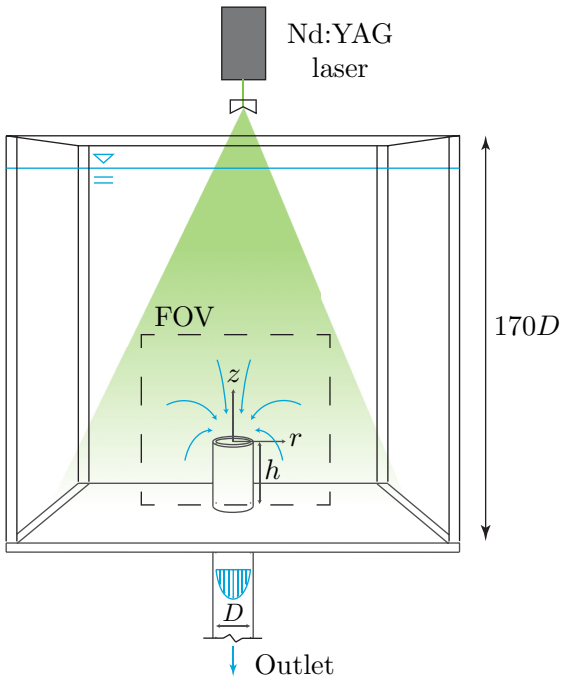

FIG. 2. Schematic of the apparatus used for experimental PIV validation of the numerical model. A camera images particles in the indicated field of view (FOV); illumination is provided by a pulsed laser sheet. A digital gear pump located far downstream of the orifice draws a constant volumetric flow rate through the inhalant tube.

D. Model validation

To validate the model, particle image velocimetry (PIV) data were collected in an acrylic tank in the r-z plane (Fig. 2). There was a round inhalant tube protruding above the bottom bed in the center of the tank and the flow was drawn into the orifice, through the tube, and to an elevated receiving reservoir by a digital gear pump with volumetric flow rate Q. The tank was roughly a cube with length, width, and depth equal to 170 diameters, minimizing the influence of the sidewalls and free surface. The working fluid (mineral oil) and inhalant tube (borosilicate glass) were index of refraction matched, enabling simultaneous characterization of both the exterior and interior flow fields.

The tank was seeded with neutrally buoyant low-Stokes-number particles (20 μm, 1.03 g/cm^3 microspheres) with 8–10 particles in the resulting interrogation subwindows [35]. A double-pulsed Nd:YAG laser (532-nm) beam was spread into a thin sheet ($\sim$500 μm) using a cylindrical diverging lens. A scientific complementary metal-oxide semiconductor (sCMOS) camera imaged particles in the laser sheet at pulse separation times that optimized particle displacements at one-quarter the width of a subwindow [35]. The image set was postprocessed using DaVis software (8.2.3, LaVision GmbH) to compute planar fluid velocity fields via fast-Fourier-transform-based cross-correlation analyses of particle displacement within subwindows between image pairs.

Due to the complexity of performing the experiments relative to running numerical simulations, PIV data were collected for a single flow case in the middle of the Re-h^* parameter space (Re = 10 and $h^* = 2$) and for a single

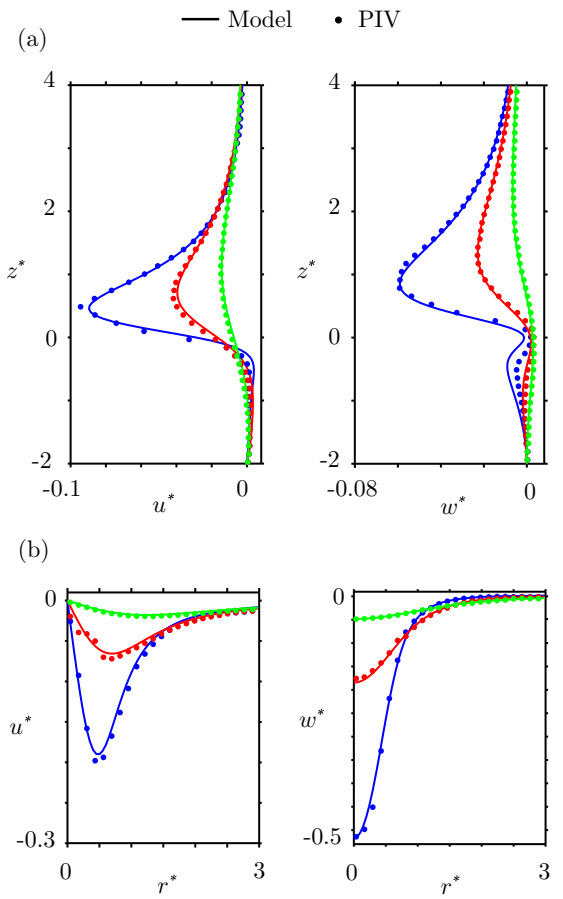

FIG. 3. Comparison of velocity profiles obtained with particle image velocimetry (symbols) and numerical simulations (lines) for Re = 10, $h^* = 2$, and $t^* = 10$: (a) axial profiles of radial (u^*, left panel) and axial (w^*, right panel) velocity components at $r^* = 1.0$ [blue (dark gray)], 1.5 [red (gray)], and 2.5 [green (light gray)] and (b) radial profiles of radial (u^*, left panel) and axial (v^*, right panel) velocity components at $z^* = 0.5$ [blue (dark gray)], 1.0 [red (gray)], and 2.0 [green (light gray)]. Note that the spatial scales are identical in (a) and (b), while the velocity scales are considerably different.

nondimensional time ($t^* = 10$). These results were used to validate the numerical model for a single representative case, permitting further numerical exploration of the local Re-h^* parameter space. Velocity data obtained experimentally and numerically are compared directly in Fig. 3. The profiles demonstrate close agreement in both velocity components (u^* and w^*) throughout the domain, including in regions of high deformation rates and velocity gradients near the inlet orifice.

III. RESULTS

Principal aims of this study are to characterize the exterior flow field of inhalant flows, to understand transient development of these flows, and to quantify the initial spatial distribution of subsequently inhaled fluid. First, the long-time behavior beyond the time scale of rapid transient development is presented in order to identify basic features of the flow field. Next, the transient response is investigated by tracking the time evolution of a region of influence (ROI) of the flow. We define

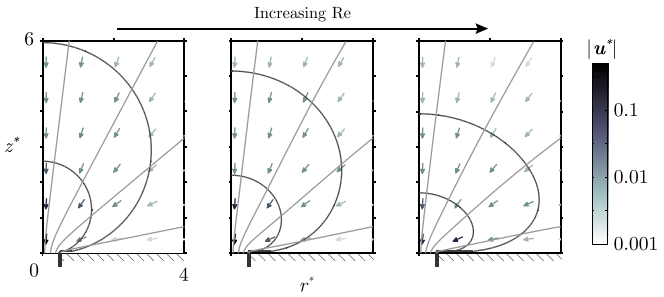

FIG. 4. Long-time behavior of the bed-flush case ($h^* = 0$) at $t^* = 100$ for Re = 1 (left panel), 10 (middle panel), and 100 (right panel). The z axis is the line of axisymmetry, the thick black line at $r^* = 0.5$ is a section of the inhalant tube sidewall, and the crosshatch at $z^* = 0$ is the solid bottom bed. Thin black lines are the 1% and 5% ROIs and gray lines are streamlines. Velocity direction and magnitude are denoted by arrow orientation and coloration, respectively.

ROIs at any instant in time as the volume of fluid bounded by a particular velocity magnitude contour. Finally, fluid inhalation volumes are quantified as a function of inhalation period. Results are presented for Re = 1, 10, and 100 and at extraction heights $h^* = 0$ (bed-flush case), $h^* = 2$ (near-bed case), and $h^* = 40$ (unbounded case).

A. Long-time behavior

To characterize basic features of the flow, we present flow fields at times large compared to the time scale of rapid transient development [(D^2/ν)/Re]; we consider flows at $t^* = 100$ as being representative of long-time behavior. Although exterior flows continue to slowly develop after $t^* = 100$, particularly for the Re = 1 case, structure of the flows becomes essentially constant. Model results at $t^* = 100$ are shown for $h^* = 0, 2$, and 40 in Figs. 4, 5, and 6, respectively. Within each figure, the Reynolds number varies from 1 (left panel) to 10 (middle panel) to 100 (right panel). Because the flow is axisymmetric about the z axis, flow fields are displayed in the r-z half plane. To best visualize the large dynamic range

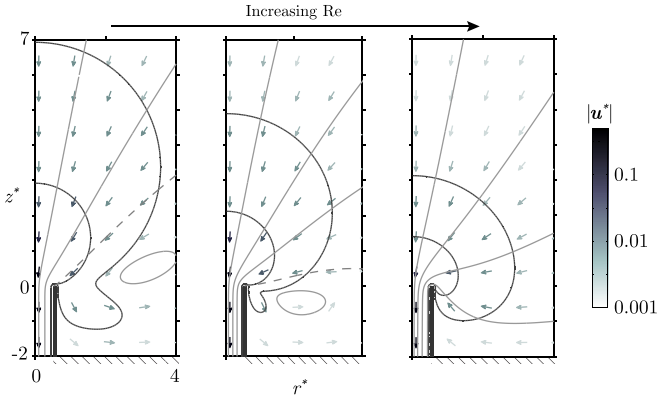

FIG. 5. Long-time behavior of the near-bed case ($h^* = 2$) at $t^* = 100$ for Re = 1 (left panel), 10 (middle panel), and 100 (right panel). Inhalant tube, bottom bed, ROIs, streamlines, and velocity vectors are represented as in Fig. 4. The Re = 1 and 10 flow fields include stagnation streamlines indicated with a dashed line.

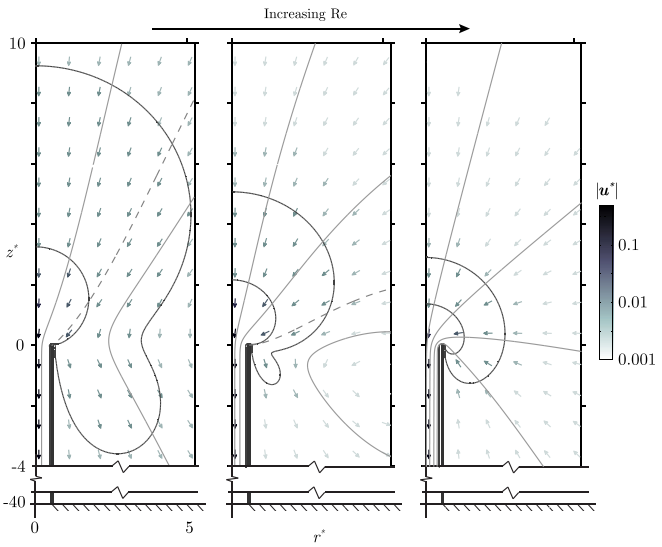

FIG. 6. Long-time behavior of the unbounded case ($h^* = 40$) at $t^* = 100$ for Re = 1 (left panel), 10 (middle panel), and 100 (right panel). Inhalant tube, bottom bed, velocity magnitude contours, streamlines, and velocity vectors are represented as in Fig. 4. Note the break in the vertical axis indicating large separation between the inlet orifice and bottom bed. The Re = 1 and 10 flow fields include stagnation streamlines (dashed lines).

in $\boldsymbol{u}^*$, velocity magnitudes are displayed on a logarithmic scale. Velocity magnitude attenuates rapidly with radial distance from the inlet orifice and decays to $|\boldsymbol{u}^*| = 0.01$ within a few inhalant tube diameters, corresponding to 1% w_o. While the velocity vectors as presented are visible down to approximately $|\boldsymbol{u}^*| = 0.002$ (0.2% w_o), these smallest velocities are likely too small to be relevant or measurable in most practical applications. To indicate the region of the flow where velocities are meaningful, we define an effective ROI at any instant in time as the volume of fluid bounded by a specific contour of $|\boldsymbol{u}^*|$. We present ROIs for $|\boldsymbol{u}^*| = 0.05$ and $|\boldsymbol{u}^*| = 0.01$, indicating where velocities have decayed to 5% and 1% of w_o (the average velocity in the inhalant tube), respectively.

In the bed-flush geometry ($h^* = 0$, Fig. 4), flow consists of radial inflow towards the inlet orifice for all Re. Inflow magnitude decays rapidly with distance from the inlet orifice in a manner reminiscent of a sink flow. At different Re, subtle flow differences are evidenced in the size and shape of the ROIs. The no-slip condition along the bottom bed gives rise to a thicker boundary layer at lower Re, flattening the 1% ROI near the bed. At low Re, this bottom boundary layer retards lateral inflow, causing preferential vertical inflow along the z axis. At high Re, thinning of the bottom boundary layer permits more omnidirectional inflow. Directional flow bias at lower Re alters the aspect ratio of the ROIs. For Re = 1, the ROIs show elongation along the z axis. This effect is somewhat mitigated at Re = 10 (middle panel) and at Re = 100 (right panel) the ROIs are very nearly hemispherical. As the most inviscid flow modeled, the Re = 100 case most closely resembles a sink flow in which the velocity contours would conform to hemispherical potential lines.

Increasing extraction height to $h^* = 2$ (near-bed case, Fig. 5) results in structural changes to the flow field, particularly at low Re. At high Reynolds number (Re = 100, right panel), there is once again radial inflow to the orifice that now includes fluid from below. At Re = 1 and 10 (left and middle panels), however, the flow bifurcates and some entrained fluid now bypasses the orifice and continues downward along the exterior inhalant tube wall and radially outward along the bottom bed. Demarcation between inhaled and bypassed fluid is a stagnation streamline that terminates on the rim of the inlet orifice, as shown in the figure (here and elsewhere we denote stagnation streamlines as dashed gray lines). Flow velocities associated with fluid that bypasses the orifice manifest as a lobe of the 1% ROI extending below the orifice. The impact of viscous entrainment is largest at the lowest Reynolds number (Re = 1, left panel), increasing the amount of bypassed fluid with a corresponding increase in size of the 1% ROI lobe. Enhanced effects of viscous diffusion at low Re are also evident in the overall increase in spatial extent of the 1% ROI. Conversely, in the most inviscid flow case (Re = 100, right panel), inward advection of momentum dominates outward viscous diffusion and the flow reverts once again to a state suggestive of an inviscid sink flow with radial inflow and nearly spherical ROIs.

For the unbounded geometry ($h^* = 40$, Fig. 6), the influence of the bottom bed is effectively eliminated. As in the $h^* = 2$ geometry, the Re = 1 and 10 flows (left and middle panels) bifurcate and some entrained fluid bypasses the orifice and is recirculated outward. As before, the stagnation streamline (dashed line) separates inhaled and bypassed fluid. For Re = 1, viscous diffusion causes the extent of the flow field to be greatly expanded. In fact, as we show later, the transient development for this viscous case continues indefinitely. These amplified diffusive effects are evidenced by substantial enlargement of the ROIs relative to the previous two geometries. Increased viscous entrainment of fluid also increases the size of the 1% ROI lobe of bypassed fluid. In the absence of the nearby bottom bed, the deflection of the lobe laterally away from the inhalant tube is reduced. The Re = 10 unbounded case (middle panel) is surprisingly similar to the corresponding near-bed case. Finally, in the most inviscid case (Re = 100, right panel), inward advection dominates outward diffusion and the flow field is once again trapped in a state reminiscent of an unbounded sink flow with nearly spherical ROIs.

B. Transient response

To characterize the transient response of the flow, we present 1% ROI contours at the impulsive start of inhalation ($t^* = 0$), through rapid transient development ($t^* = 1$), and into the long-time behavior ($t^* = 100$). Model results are shown for $h^* = 0$, 2, and 40 in Figs. 7, 8, and 9, respectively, for Re = 1 (left panels), Re = 10 (middle panels), and Re = 100 (right panels). The $t^* = 100$ ROI contours here correspond to long-time results in the preceding section.

Conceptually, the transient response of the exterior flow can be decomposed into the sum of two separate components. First, an inviscid elliptic baseline component that sets up instantaneously and is reminiscent of the steady sink flow, but must satisfy the no-slip boundary conditions along solid surfaces and must match the distributed and directional flow

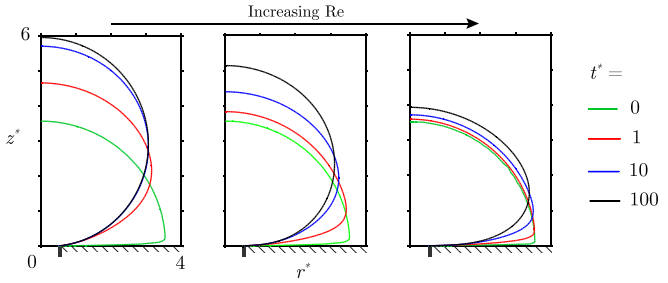

FIG. 7. Transient development of the flow field as represented by 1% ROI contours for the bed-flush geometry ($h^* = 0$) at Re = 1 (left panel), 10 (middle panel), and 100 (right panel).

at the orifice. Second, a viscous component diffuses radially outward over time. The relative strength and interplay of these two components depends on nondimensional time, Re, and h^*.

At $t^* = 0$, flow consists entirely of the inviscid elliptic response that is insensitive to Re for any particular geometry and associated boundary conditions. Figures 7–9 confirm that the $t^* = 0$ ROIs at Re = 1 (left panels) are identical to those at Re = 10 (middle panels) and Re = 100 (right panels). For $t^* \geqslant 0$, the unsteady viscous component of the transient propagates radially outward from the orifice. Because the time scale for the transient development goes as $(D^2/\nu)/\mathrm{Re}$, the transient develops 100 times faster at Re = 100 when compared to Re = 1 (for constant D and ν). Furthermore, at high Re the component of the transient is relatively weak and the elliptic inviscid component dominates. Again, Figs. 7–9 confirm that ROIs for the most inviscid flow (Re = 100, right panels) are nearly identical for all four t^* values shown, indicating that the flow is trapped in a state dominated by the sinklike inviscid component. For the intermediate case (Re = 10, middle panels), the increased relative importance of viscous diffusive effects causes the ROIs to enlarge and propagate further relative to the most inviscid flow at a given h^*. Finally, for the most viscous flow at Re = 1, the viscous transient component becomes dominant and the flow evolves continuously in time. As h^* increases and the influence of the bottom bed is reduced, the effects of the viscous transient

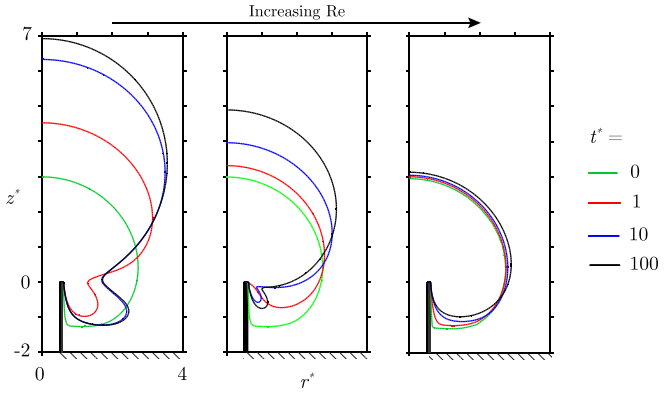

FIG. 8. Transient development of the flow field as represented by 1% ROI contours for the near-bed geometry ($h^* = 2$) at Re = 1 (left panel), 10 (middle panel), and 100 (right panel).

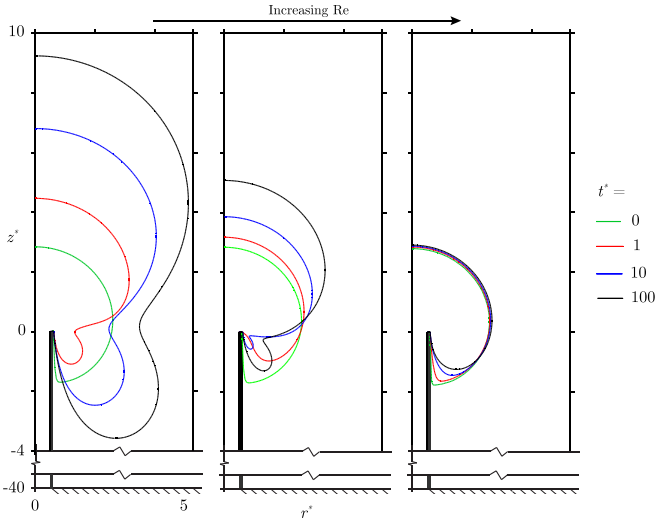

FIG. 9. Transient development of the flow field as represented by 1% ROI contours for the unbounded geometry ($h^* = 40$) at Re = 1 (left panel), 10 (middle panel), and 100 (right panel). Note the break in the vertical axis indicating large separation between the inlet orifice and bottom bed.

component at Re = 1 (left panels) are increased and the ROIs grow larger and propagate further. In contrast, the spatial extent of the ROIs for the intermediate (Re = 10, middle panels) and most inviscid (Re = 100, right panels) flows are insensitive to h^*. These differences in the transient response from the most viscous flow (Re = 1) to the most inviscid (Re = 100) again emphasize a fundamental feature of the flow: the competition between advection of momentum towards the orifice and viscous diffusion away from the orifice.

C. Inhalation volumes

Here we investigate the initial spatial distribution of fluid that is subsequently ingested into the inhalant tube. We represent these inhalation volumes by their bounding envelopes (Fig. 10). These volumes were computed with inhalation beginning at $t^* = 100$ (corresponding to the long-time behavior of the flow) and proceeding for inhalation durations $\Delta t^* = 1$, 10, and 100. An inhalation duration $\Delta t^* = 1$ corresponds to the time required to inhale a characteristic volume $(\pi D^3/4Q)$; this is equivalent to a cylinder with diameter and length equal to D. Sizes of inhalant volumes for a given nondimensional inhalation duration Δt^* are therefore identical (regardless of Re or h^*). That is, all blue (dark gray) envelopes in Fig. 10 represent equal volumes. Although the two-dimensional envelopes for a given Δt^* do not necessarily have equal areas, they sweep out equal volumes when rotated around the line of axisymmetry (z axis). Representative streamlines at $t^* = 100$ are shown in gray; flow continues to develop over time, but the change is negligible over the inhalation durations used. For cases that have a stagnation streamline (four lower left panels; see also Figs. 5 and 6), a portion of the inhalation volume envelope along the bottom coincides with this streamline (shown with a dashed line). Fluid below this streamline is recirculated outward and can

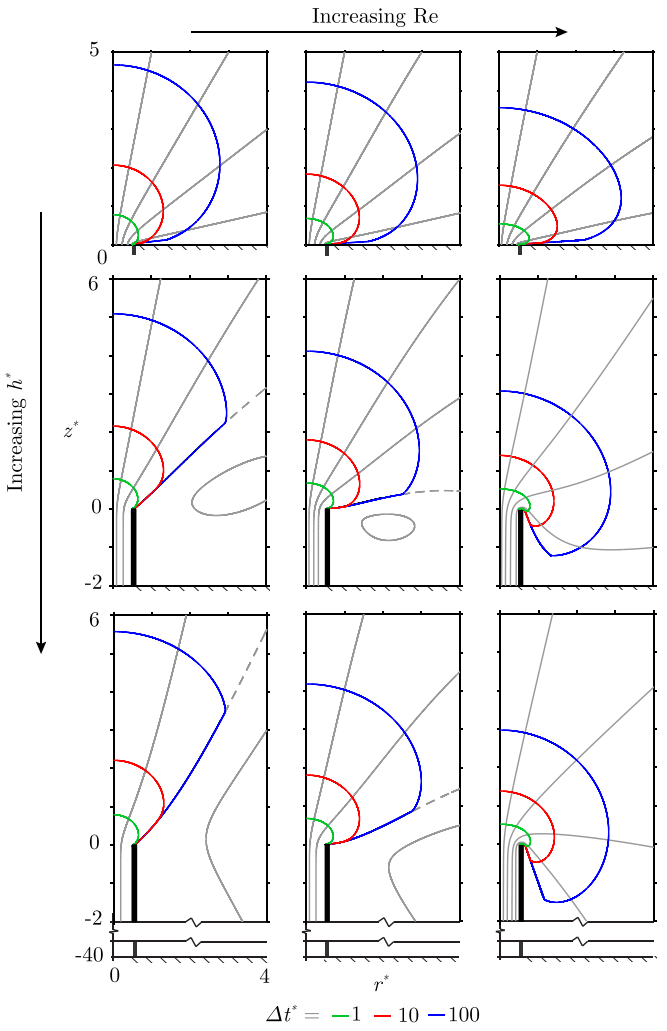

FIG. 10. Inhalation volume envelopes for durations of $\Delta t^* = 1$, 10, and 100. Reynolds number Re increases from 1 (left column) to 10 (middle column) to 100 (right column) and h^* increases from 0 (top row) to 2 (middle row) to 40 (bottom row). Streamlines are shown in gray. For the four lower left panels, the bottom boundary of the inhalation volume coincides with a stagnation streamline (dashed line) as discussed in the text.

never enter the orifice. In contrast, for the $h^* = 0$ (top row) and the Re = 100 (right column) cases all flow is radially inward and as $\Delta t^* \to \infty$ the envelopes expand to fill the entire domain.

Inhalant volumes show strong directional bias as a function of not only Re (columns) but also extraction height h^* (rows) and depart significantly from what would be predicted by potential flow theory (Fig. 10). For the most viscous case (Re = 1, left column), increasing h^* shifts inhalant volumes up towards the axis of the inhalant tube, producing directional inhalation. Conversely, for the most inviscid case (Re = 100, right column), we see the exact opposite: Increasing h^* now enables a more omnidirectional inhalation. For the intermediate case (Re = 10, middle column), the shape of the inhalation volume is relatively insensitive to h^*. The most striking departure from potential flow theory occurs at Re = 1 and $h^* = 40$ (lower left panel). For this viscous case, downward momentum from the directional flow in the inhalant tube diffuses readily throughout the exterior domain. In the absence of a nearby bed, this diffusion activates a systemic downward flow (see the left panel in Fig. 6), much of which must bypass the orifice (as evidenced by the upward deflection of the stagnation streamline). This produces a conical inhalation volume that samples preferentially from above. Overall, the choice of Re and h^* is seen to have profound impact on the spatial distribution of inhaled fluid.

IV. SUMMARY

Potential flow theory has been historically used to approximate flows approaching an orifice as inviscid sink flows. However, many inhalant flows are not well described by potential flow theory because they are subject to boundary conditions that are both directional and spatially distributed and their development is influenced by viscous diffusion of momentum. In this study we characterized transient hydrodynamics of impulsively started, laminar inhalant flows approaching an orifice for a range of Reynolds numbers (to vary the influence of viscous effects) and extraction heights (to vary the influence of the solid bed). The increasing importance of viscosity at lower Re is evidenced in our results by significant departures from potential flow theory.

For all Re, the flow at $t^* \ll 1$ is sinklike, representing the inviscid elliptic response. For high Re, the flow remains relatively similar to the sink flow for all times. At lower Re, increased viscous effects entrain an ever-growing volume of fluid and the flow continues to develop indefinitely. In some cases, flows at lower Re spatially bifurcate, causing some fluid to be inhaled and other fluid to bypass the orifice. The demarcation line between inhaled and bypassed fluid is a stagnation streamline that terminates on the rim of the orifice. The viscous diffusive effects seen at lower Re are further enhanced with increasing extraction height, whereas the higher-Re flows remain trapped in a sinklike state regardless of h^*.

The structural changes in the fluid inhalation volumes as a function of Re and h^* are analogous to those in the ROIs. For lower Re, increasing h^* shifts inhalant volumes towards the axis of the inhalant tube, producing more directional inhalation. In contrast, at higher Re, increasing h^* has the opposite effect and produces a more omnidirectional inhalation. Strong directional bias in inhalation as a function of Re and h^* could be exploited by organisms and engineers alike to achieve specific inhalation criteria. For example, a bottom-dwelling siphon-feeding organism might decrease its pumping Re and increase its tube height to sample more directionally from above and inhale food- and oxygen-rich fluid volumes farther removed from the bottom bed. However, this pumping regime will also produce the greatest spatial extent of the region of influence of the flow, perhaps making the organism more detectable to nearby predators. Similarly, engineers and scientists may require fluid samplers capable of both isotropic and anisotropic sampling regimes depending on environmental conditions or design criteria; this could be achieved by adjusting Reynolds number and extraction height to suit sampling needs of a specific application.

ACKNOWLEDGMENTS

This work was supported by the National Science Foundation (USA), under Grant No. OCE 1260199 to J.P.C. We acknowledge and thank Pete Jumars for motivation to investigate these flows and for fruitful interactions and discussions.

[1] A. Potter and F. H. Barnes, Phys. Educ. **6**, 362 (1971).
[2] K. V. Singarajah, J. Exp. Mar. Biol. Ecol. **3**, 171 (1969).
[3] S. G. Monismith, J. R. Koseff, J. K. Thompson, C. A. O'Riordan, and H. M. Nepf, Limnol. Oceanogr. **35**, 680 (1990).
[4] P. A. Jumars, Limnol. Oceanogr.: Fluids Environ. **3**, 21 (2013).
[5] R. C. Schroter and M. F. Sudlow, Respir. Physiol. **7**, 341 (1969).
[6] P. Cole, Am. J. Rhinol. **14**, 245 (2000).
[7] J. L. Gay-Lussac, *Instruction sur l'Essai du Chlorure de Chaux* (Thuau, Paris, 1830).
[8] A. T. Shohl, J. Am. Chem. Soc. **50**, 417 (1928).
[9] M. Köhn, Ph.D. thesis, Forstliche Hochschule Eberswalde, 1928.
[10] H. E. Lewis, A. R. Foster, B. J. Mullan, R. N. Cox, and R. P. Clark, Lancet **293**, 1273 (1969).
[11] G. S. Settles, J. Fluids Eng. **127**, 189 (2005).
[12] S. K. Zaripov, L. M. Zigangareeva, and O. M. Kiselev, Fluid Dyn. **35**, 242 (2000).
[13] S. J. Dunnett and X. Wen, J. Aerosol Sci. **33**, 1653 (2002).
[14] B. L. Smith and G. W. Swift, Exp. Fluids **34**, 467 (2003).
[15] E. A. Variano, E. Bodenschatz, and E. A. Cowen, Exp. Fluids **37**, 613 (2004).
[16] S. Van Wassenbergh and P. Aerts, J. R. Soc. Interface **6**, 149 (2009).
[17] S. Yaniv, D. Elad, and R. Holzman, J. Exp. Biol. **217**, 3748 (2014).
[18] C. B. Jorgensen, P. Famme, H. S. Kristensen, P. S. Larsen, F. Møhlenber, and H. U. Riisgård, Mar. Ecol. Prog. Ser. **34**, 69 (1986).
[19] H. U. Riisgård and P. S. Larsen, Biol. Rev. Cambridge Philos. Soc. **70**, 67 (1995).
[20] L. Rosenhead, in *Laminar Boundary Layers: An Account of the Development, Structure, and Stability of Laminar Boundary Layers in Incompressible Fluids, Together with a Description of the Associated Experimental Techniques*, edited by L. Rosenhead (Clarendon, Gloucestershire, 1963), p. 428.
[21] P. K. Kundu, I. M. Cohen, and H. H. Hu, *Fluid Mechanics*, 3rd ed. (Elsevier Academic, San Diego, 2004), p. 280.
[22] L. G. Whitehead and G. S. Canetti, Philos. Mag. **41**, 988 (1950).
[23] F. Durst, S. Ray, B. Ünsal, and O. A. Bayoumi, J. Fluids Eng. **127**, 1154 (2005).
[24] B. Atkinson, M. P. Brocklebank, C. C. H. Card, and J. M. Smith, AIChE J. **15**, 548 (1969).
[25] R. Y. Chen, J. Fluids Eng. **95**, 153 (1973).
[26] R. K. Shah, J. Fluids Eng. **100**, 177 (1978).
[27] S. P. Sutera and R. Skalak, Annu. Rev. Fluid Mech. **25**, 1 (1993).
[28] F. M. White and I. Corfield, *Viscous Fluid Flow* (McGraw-Hill, New York, 2006), Vol. 3.
[29] P. M. Gresho and R. L. Sani, *Incompressible Flow and the Finite Element Method: Isothermal Laminar Flow* (Wiley, Hoboken, 1998), Vol. 2.
[30] R. K. Brayton, F. G. Gustavson, and G. D. Hachtel, Proc. IEEE **60**, 98 (1972).
[31] A. C. Hindmarsh, P. N. Brown, K. E. Grant, S. L. Lee, R. Serban, D. E. Shumaker, and C. S. Woodward, ACM Trans. Math. Software **31**, 363 (2005).
[32] O. Schenk, K. Gärtner, W. Fichtner, and A. Stricker, Future Gen. Comput. Syst. **18**, 69 (2001).
[33] O. Schenk and K. Gärtner, Future Gen. Comput. Syst. **20**, 475 (2004).
[34] R. L. Panton, *Incompressible Flow*, 4th ed. (Wiley, Hoboken, 2013).
[35] M. Raffel, C. E. Willert, S. Wereley, and J. Kompenhans, *Particle Image Velocimetry: A Practical Guide*, 2nd ed. (Springer, Berlin, 2007).